Research Article | Vol. 26, No. 16 | 6 Aug 2018 | OPTICS EXPRESS 20758
Optics EXPRESS

Ultrathin graphene diaphragm-based extrinsic Fabry-Perot interferometer for ultra-wideband fiber optic acoustic sensing

Wenjun Ni,[1,2,3,4] Ping Lu,[1,*] Xin Fu,[1] Wei Zhang,[1] Perry Ping Shum,[2,3] Handong Sun,[4] Chunyong Yang,[5] Deming Liu,[1] and Jiangshan Zhang[6]

[1]*Wuhan National Laboratory for Optoelectronics(WNLO), National Engineering Laboratory for Next Generation Internet Access System, School of Optical and Electronic Information, Huazhong University of Science and Technology, Wuhan 430074, China*
[2]*School of Electrical and Electronic Engineering, Nanyang Technological University, 639798, Singapore*
[3]*CINTRA CNRS/NTU/THALES, UMI 3288, Research Techno Plaza, 50 Nanyang Drive, Nanyang Technological University, 637553, Singapore*
[4]*School of Physical and Mathematical Sciences, Nanyang Technological University, 637371, Singapore*
[5]*Hubei Key Laboratory of Intelligent Wireless Communications, College of Electronics and Information Engineering, South-Central University for Nationalities, Wuhan, 430074, China*
[6]*Schoolof Electronic Information and Communications, Huazhong University of Science and Technology, Wuhan 430074, China*
**pluriver@mail.hust.edu.cn*

Abstract: An ultra-wideband fiber optic acoustic sensor based on graphene diaphragm with a thickness of 10nm has been proposed and experimentally demonstrated. The two reflectors of the extrinsic Fabry-Perot interferometer is consist of fiber endface and graphene diaphragm, and the cavity is like a horn-shape. The radius of the effective area of the ultrathin graphene diaphragm is 1mm. Attributed to the strong van der Waals force between the diaphragm and the ceramic ferrule, the sensor head can be applied not only in the air but also underwater. Experimental results illustrate that ultra-wideband frequency response is from 5Hz to 0.8MHz, covering the range from infrasound to ultrasound. The noise-limited minimum detectable pressure level of 0.77Pa/Hz$^{1/2}$@5Hz and 33.97μPa/Hz$^{1/2}$@10kHz can be achieved, and the applied sound pressure is 114dB and 65.8dB, respectively. The fiber optic acoustic sensor may have a great potential in seismic wave monitoring, photoacoustic spectroscopy and photoacoustic imaging application due to its compact structure, simple manufacturing, and low cost.

OCIS codes: (060.2370) Fiber optics sensors; (050.2230) Fabry-Perot; (280.4788) Optical sensing and sensors; (230.1040) Acousto-optical devices.

References and links

1. M. Ichihara, M. Takeo, A. Yokoo, J. Oikawa, and T. Ohminato, "Monitoring volcanic activity using correlation patterns between infrasound and ground motion," Geophys. Res. Lett. **39**(4), 6856–6860 (2012).
2. Y. Cao, W. Jin, H. L. Ho, and J. Ma, "Miniature fiber-tip photoacoustic spectrometer for trace gas detection," Opt. Lett. **38**(4), 434–436 (2013).
3. J. Zhu, L. Ren, S. C. Ho, Z. Jia, and G. Song, "Gas pipeline leakage detection based on PZT sensors," Smart Mater. Struct. **26**(2), 025022 (2017).
4. A. P. Jathoul, J. Laufer, O. Ogunlade, B. Treeby, B. Cox, E. Zhang, P. Johnson, A. R. Pizzey, B. Philip, T. Marafioti, M. F. Lythgoe, R. B. Pedley, M. A. Pule, and P. Beard, "Deep in vivo photoacoustic imaging of mammalian tissues using a tyrosinase-based genetic reporter," Nat. Photonics **9**(4), 239–246 (2015).
5. H. F. Zhang, K. Maslov, G. Stoica, and L. V. Wang, "Functional photoacoustic microscopy for high-resolution and noninvasive in vivo imaging," Nat. Biotechnol. **24**(7), 848–851 (2006).
6. M. Han, T. Liu, L. Hu, and Q. Zhang, "Intensity-demodulated fiber-ring laser sensor system for acoustic emission detection," Opt. Express **21**(24), 29269–29276 (2013).

#334962 https://doi.org/10.1364/OE.26.020758
Journal © 2018 Received 13 Jun 2018; revised 15 Jul 2018; accepted 20 Jul 2018; published 30 Jul 2018

Optics EXPRESS

7. B. Xu, Y. Li, M. Sun, Z. W. Zhang, X. Y. Dong, Z. X. Zhang, and S. Z. Jin, "Acoustic vibration sensor based on nonadiabatic tapered fibers," Opt. Lett. **37**(22), 4768–4770 (2012).
8. Y. Li, X. Wang, and X. Bao, "Sensitive acoustic vibration sensor using single-mode fiber tapers," Appl. Opt. **50**(13), 1873–1878 (2011).
9. W. Ni, P. Lu, X. Fu, S. Wang, Y. Sun, D. Liu, and J. Zhang, "Highly sensitive optical fiber curvature and acoustic sensor based on thin core ultralong period fiber grating," IEEE Photonics J. **9**(2), 7100909 (2017).
10. D. Pawar, C. N. Rao, R. K. Choubey, and S. N. Kale, "Mach-Zehnder interferometric photonic crystal fiber for low acoustic frequency detections," Appl. Phys. Lett. **108**(4), 041912 (2016).
11. L. Liu, P. Lu, H. Liao, S. Wang, W. Yang, D. Liu, and J. Zhang, "Fiber-optic michelson interferometric acoustic sensor based on a PP/PET diaphragm," IEEE Sens. J. **16**(9), 3054–3058 (2016).
12. Z. Gong, K. Chen, X. Zhou, Y. Yang, Z. Zhao, H. Zou, and Q. Yu, "High-sensitivity Fabry-Perot interferometric acoustic sensor for low-frequency acoustic pressure detections," J. Lightwave Technol. **35**(24), 5276–5279 (2017).
13. F. Wang, Z. Shao, J. Xie, Z. Hu, H. Luo, and Y. Hu, "Extrinsic Fabry–Pérot underwater acoustic sensor based on micromachined center-embossed diaphragm," J. Lightwave Technol. **32**(23), 4026–4034 (2014).
14. Q. Rong, Z. Shao, X. Yin, T. Gang, F. Liu, A. Sun, and X. Qiao, "Ultrasonic imaging of seismic physical models using fiber bragg grating fabry–perot probe," IEEE J. Sel. Top. Quantum. **23**(2), 223–228 (2017).
15. D. H. Wang, S. J. Wang, and P. G. Jia, "In-line silica capillary tube all-silica fiber-optic Fabry-Perot interferometric sensor for detecting high intensity focused ultrasound fields," Opt. Lett. **37**(11), 2046–2048 (2012).
16. Z. Shao, Q. Rong, F. Chen, and X. Qiao, "High-spatial-resolution ultrasonic sensor using a micro suspended-core fiber," Opt. Express **26**(8), 10820–10832 (2018).
17. S. Wang, P. Lu, L. Liu, H. Liao, Y. Sun, W. Ni, X. Fu, X. Jiang, D. Liu, J. Zhang, H. Xu, Q. Yao, and Y. Chen, "An infrasound sensor based on extrinsic fiber-optic Fabry–Perot interferometer structure," IEEE Photonics Technol. Lett. **28**(11), 1264–1267 (2016).
18. L. Liu, P. Lu, S. Wang, X. Fu, Y. Sun, D. Liu, J. Zhang, H. Xu, and Q. Yao, "UV adhesive diaphragm-based FPI sensor for very-low-frequency acous tic sensing," IEEE Photonics J. **8**(1), 6800709 (2016).
19. S. Dass and R. Jha, "Tapered fiber attached nitrile diaphragm-based acoustic sensor," J. Lightwave Technol. **35**(24), 5411–5417 (2017).
20. F. Xu, J. Shi, K. Gong, H. Li, R. Hui, and B. Yu, "Fiber-optic acoustic pressure sensor based on large-area nanolayer silver diaghragm," Opt. Lett. **39**(10), 2838–2840 (2014).
21. F. Guo, T. Fink, M. Han, L. Koester, J. Turner, and J. Huang, "High-sensitivity, high-frequency extrinsic Fabry-Perot interferometric fiber-tip sensor based on a thin silver diaphragm," Opt. Lett. **37**(9), 1505–1507 (2012).
22. H. Liao, P. Lu, L. Liu, S. Wang, W. Ni, X. Fu, D. Liu, and J. Zhang, "Phase Demodulation of Short-Cavity Fabry–Perot Interferometric Acoustic Sensors With Two Wavelengths," IEEE Photonics J. **9**(2), 7102207 (2017).
23. Y. Wu, C. Yu, F. Wu, C. Li, J. Zhou, Y. Gong, Y. Rao, and Y. Chen, "A Highly Sensitive Fiber-Optic Microphone Based on Graphene Oxide Membrane," J. Lightwave Technol. **35**(19), 4344–4349 (2017).
24. J. Ma, W. Jin, H. Xuan, C. Wang, and H. L. Ho, "Fiber-optic ferrule-top nanomechanical resonator with multilayer graphene film," Opt. Lett. **39**(16), 4769–4772 (2014).
25. F. Yu, Q. Liu, X. Gan, M. Hu, T. Zhang, C. Li, F. Kang, M. Terrones, and R. Lv, "Ultrasensitive Pressure Detection of Few-Layer MoS_2," Adv. Mater. **29**(4), 1603266 (2017).
26. B. Fischer, "Optical microphone hears ultrasound," Nat. Photonics **10**(6), 356–358 (2016).
27. D. Giovanni, *Flat and Corrugated Diaphragm Design Handbook* (Marcel Dekker, 1982).
28. J. Ma, *Miniature Fiber-Tip Fabry-Perot Interferometric Sensors for Pressure and Acoustic Detection* (Hong Kong Polytechnic University-Dissertations, 2014), Chap. 3.

1. Introduction

Fiber optic acoustic sensors (FOAS) have attracted more and more attention due to their important role in modern society. The acoustic wave has a wide frequency range that extends from infrasound (<20Hz) up to ultrasound (>20kHz), and the measurement of acoustic waves at different frequency bands has different applications. It mainly focuses on military and civilian areas, such as anti-submarine surveillance [1], photoacoustic spectroscopy [2], oil and gas pipeline leakage monitoring [3], and photoacoustic imaging [4,5]. Various fiber-based acoustic sensors have been reported at present, such as fiber optic interferometers, FBG-based fiber laser and other passive optical fiber devices, especially couplers and tapers. FBG-based fiber laser [6] is mainly for ultrasound measurement through the transducer of composite sheet. Tapers [7], couplers [8] and LPFG [9] need to be pasted on the transducer, thus a relatively larger size of membrane is indispensable. The most common interferometers employed to FOAS are Mach-Zehnder (MZ) [10], Michelson interferometer (MI) [11] and Fabry-Pérot (FP) [12,13]. The sensing principles of MZ and MI are similar, and both of the

Optics EXPRESS

two interferometers are greatly affected by external temperature and polarization fading because of the long arm length. As a result, FP has become a research hotspot owing to its compact structure and simple fabrication.

Recently, most kinds of fiber FP-based structures have been widely applied to acoustic sensing, and they can be divided into two categories: intrinsic and extrinsic cavity. The former is all fiber structure, such as FBG-FP [14], hollow core fiber FP (HCF-FP) [15] or other special fiber FP [16]. However, the measured frequency bands of the aforementioned intrinsic FP structure are not wide. In order to broaden response range, diaphragm-based extrinsic FP interferometer (EFPI) has become become more and more popular. The keypoint for the EFPI is the selection of transducer material. Currently, a variety of membrane materials are used to detect acoustic waves, which can be mainly classified as three categories. One of them is polymer film, such as polyethyleneterephthalate (PET) [17], ultraviolet glue [18] and nitrile [19]. The second one is metal diaphragm, such as silver [20,21] and aluminium [22]. The last one is two-dimensional (2D) material film, such as graphene [23,24] and molybdenum disulfide (MoS_2) [25]. It is difficult for polymer film to realize ultra-wideband measurement due to the relatively large thickness and low sensitivity. Similarly, the metal film requires a large area to achieve high sensitivity and large wideband. Therefore, the transducer based on 2D material is becoming a research hotspot attributed to the characteristics of ultrathin thickness and appropriate optical reflectivity.

In our work, a compact, cost-effective and ultra-wideband FOAS has been proposed and experimentally demonstrated. The sensor head is an EFPI structure based on graphene film with the thickness and radius of 10nm and 1mm, respectively. Besides, the whole length of the sensor head is only 14mm. The proposed FOAS can implement the ultra-wideband frequency response from 5Hz to 0.8MHz. The noise-limited minimum detectable pressure (MDP) level of 0.77Pa/Hz$^{1/2}$@5Hz and 33.97μPa/Hz$^{1/2}$@10kHz is achieved. Moreover, the fabricated EFPI can be measured both in air and underwater owing to the closed air cavity. To the best of our knowledge, the FOAS based on diaphragm transducer has not been reported whose frequency response range is from infrasound to ultrasound. Only the membrane-free optical microphone has achieved the frequency response from 5Hz to 1MHz [26], while this sensor is not suitable for the underwater measurement at this frequency range. Besides, it is also easy to be affected by the external vibration since the FP cavity is configured by two fixed reflectors. As a consequence, the proposed sensor will have a good prospect in ultra-wideband acoustic signal monitoring.

2. Fiber acoustic sensing mechanisms

The acoustic wave is a dynamic signal that needs to be transformed into detectable physical parameter. Thus the diaphragm transducer is essential to the EFPI structure. As illustrated in Fig. 1(a), the diaphragm will have a deformation when the acoustic waves are loaded. Therefore, the acoustic waves are turned into the vibration of the diaphragm, and the two frequencies are synchronous. That is, the acoustic signal is finally converted to the periodical variation of cavity length of EFPI.

Under the assumption of small deformations (the deformation occurred is less than 30% of the thickness of the diaphragm), the deformation of the elastic diaphragm and external pressure will have a good linearity. Whereafter, the deformation of the diaphragm vibration equation can be written as Eq. (1) [27]:

$$D_0\nabla^4\eta+\rho h\frac{\partial^2\eta}{\partial t^2}+\nu\frac{\partial\eta}{\partial t}=p_a e^{j\omega t} \tag{1}$$

where η , ρ , h are the deformation, mass density and thickness of the diaphragm, respectively. ν represents the damping coefficient of forced vibration, and p_a is the amplitude of the acoustic pressure. $D_0=Eh^3/12(1-\mu^2)$ depicts the bending stiffness of the diaphragm,

Optics EXPRESS

and $\omega=2\pi f$ represents the circular frequency of the acoustic wave. Besides, f is the frequency of the acoustic wave loaded on the diaphragm.

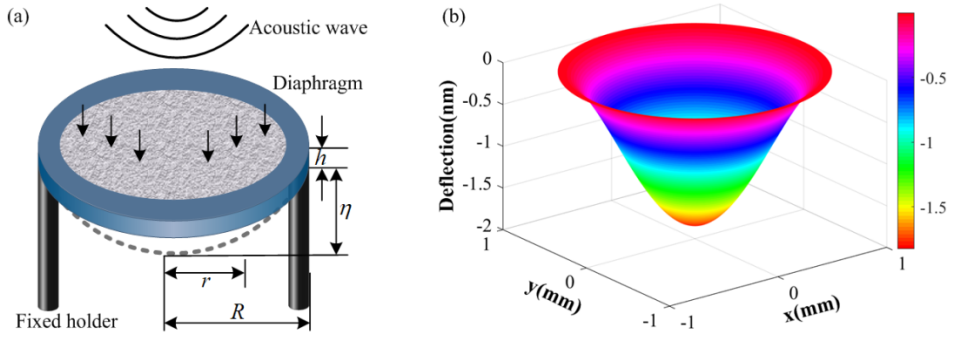

Fig. 1. (a) The schematic diagram of the acoustic wave loaded on the diaphragm. (b) The relationship between the deformation and the radial distance.

Equation (1) in polar coordinates can be expressed as:

$$D_0(\frac{\partial^2}{\partial r^2}+\frac{1}{r}\frac{\partial}{\partial r}+\frac{1}{r^2}\frac{\partial^2}{\partial \theta^2})(\frac{\partial^2}{\partial r^2}+\frac{1}{r}\frac{\partial}{\partial r}+\frac{1}{r^2}\frac{\partial^2}{\partial \theta^2})\eta+\rho h\frac{\partial^2}{\partial t^2}+\xi\frac{\partial \eta}{\partial t}=p_a e^{j\omega t} \quad (2)$$

In view of the circular diaphragm with fixed boundaries, boundary conditions are $\eta|_{r=R}=0$ and $\partial\eta/\partial r|_{r=R}=0$. Then combining Eq. (1) with Eq. (2), the deformation of the diaphragm can be deduced as:

$$\eta_{mn}=\frac{3p_a(1-\mu^2)(R^2-r^2)^2}{16Eh^3}\frac{f_{mn}^2}{\sqrt{(f_{mn}^2-f^2)^2+4f^2\xi^2}} \quad (3)$$

where μ, E, R respectively represents the Poisson's ratio, Young's modulus, and radius of the diaphragm. ξ is set as $\nu/(2\rho h)$, and r is the radial distance from the diaphragm center. f_{mn} stands for the resonant frequency of mn order mode, which can be described as [28]:

$$f_{mn}=\frac{k_{mn}^2 h}{4\pi R^2}\sqrt{\frac{E}{3\rho(1-\mu^2)}} \quad (4)$$

where k_{mn} is a constant coefficient, and the value depends on the mn order mode. It can be seen from Fig. 1(b) that the deformation is decreasing with the increasing radial distance. In general, the FOAS based on EFPI structure is always only interested in the maximum deformation point which is located at $r=0$. Consequently, the response sensitivity of acoustic pressure can be given as:

$$S_a=\frac{\partial \eta_{mn}}{\partial p}=\frac{3(1-\mu^2)R^4}{16Eh^3}\frac{f_{mn}^2}{\sqrt{(f_{mn}^2-f^2)^2+4f^2\xi^2}} \quad (5)$$

The sensitivity of the sound pressure level is defined as $S=20\lg(S_a/S_r)$, and the $S_r=1nm/Pa$ is the reference sensitivity. In terms of the graphene diaphragm, the μ, E, ρ and ν are 0.165, 1TPa, 2.2 × 10^3kg/m^3 and 0.17, respectively. Thence, the fundamental resonance frequency f_{00} can be figured out under the condition of $m=n=0$. k_{00} is equal to 3.196 which can be acquired by form enquiry. In our work, the thickness of graphene diaphragm is set as 10nm, and the detail analysis of the thickness selection is presented in section 3. So the sound pressure response curves of different working frequencies and

Optics EXPRESS

diaphragm radiuses can be obtained, as shown in Fig. 2(a). It is obvious that the maximum response point is located at the resonant frequency. As is known, the flat response area should be less than one third of the resonant frequency or three times higher. Thus, the flat response range can be controlled by adjusting the location of the resonant frequency. It can be seen from the illustration in Fig. 2(a), the smaller the diaphragm radius is, the wider the low frequency flat response region will be. The resonant frequency has a sharp increase when the radius is less than 0.3mm, and approximately flattens out when the radius is higher than 1mm. That is, an ultra-wideband flat response region can be achieved as the radius of the diaphragm increases infinitely, and it also can be observed in Fig. 2(b). Nevertheless, the sensor size is often required to be compact in practical applications. As a trade-off, the radius of the diaphragm is determined to be 1mm.

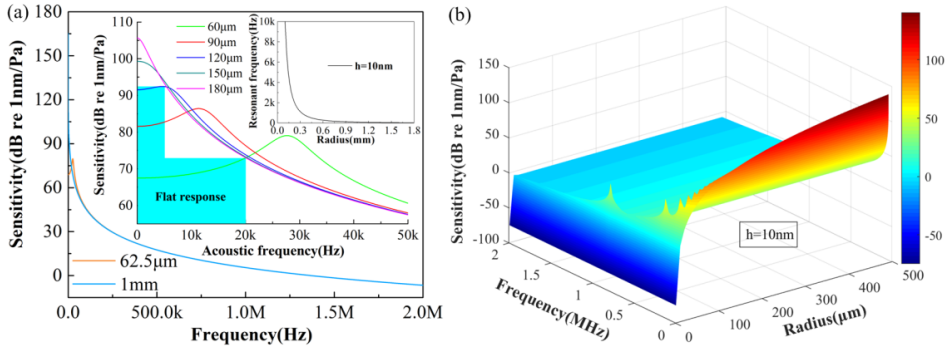

Fig. 2. (a) Sound pressure response curves of different working frequencies and diaphragm radius under the condition of h = 10nm. (b) A three-dimensional (3D) diagram of the sound pressure response.

3. Sensor fabrication and spectral analysis

The sensor head is based on the EFPI structure, as shown in Fig. 3(a). The two reflection mirrors of FP are composed of graphene diaphragm and fiber endface, and the air cavity is like a horn-shape. It should be noticed that ultrathin graphene diaphragm fabricated by chemical vapor deposition (CVD) method must be flat. The graphene diaphragm samples need to be corroded by ferric chloride solution since it is grown on the nickel substrate. After the substrate is corroded, the graphene diaphragm must be washed by deionized water to remove the residual iron ions. Whereafter, transferring the graphene diaphragm onto the endface of ceramic ferrule is the most important step in the whole fabrication process. The ceramic ferrule is vertically moved upward until it reaches the graphene diaphragm floating on the surface of the water, as displayed in Fig. 3(b). After the transfer process, the diaphragm will have a pre-bending owing to the action of gravity, and the working sketch is exhibited in Fig. 3(c). The sensor head must be placed vertically for 48 hours at room temperature of 25°C since it is removed from the water. Once the sensor head is dried, the graphene diaphragm will stick firmly on the endface of ceramic ferrule attributed to the strong van der Waals force. That is, the endface of ceramic ferrule is integrated with the graphene diaphragm. Finally, the tail fiber needs to be fixed by epoxy glue, and the whole length of the sensor head is approximate 14mm, as indicated in Fig. 3(d).

Optics EXPRESS

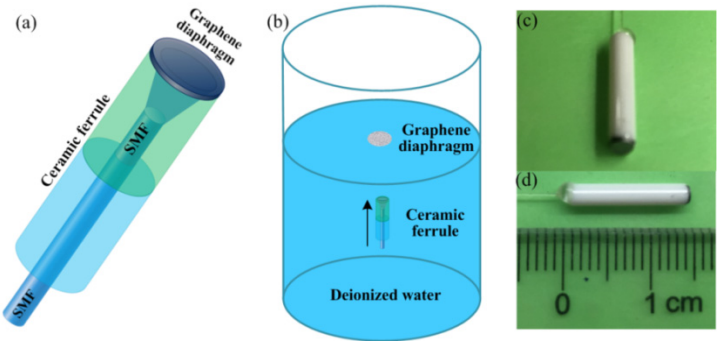

Fig. 3. (a) The schematic diagram of the sensor head based on graphene diaphragm. (b) Transferring the graphene diaphragm onto the endface of ceramic ferrule. (c) The working sketch of the sensor head. (d) The whole length of the sensor head is 14mm.

In order to better demodulate the acoustic signal, an optimal reflective spectrum is necessary. The contrast and free spectrum range (FSR) are mainly dependent on the FP cavity length and the flatness of the diaphragm. The reflectivity of the graphene diaphragm needs to match the Fresnel reflectivity of fiber endface, which is close to 4%. Taken the spatial loss of the air cavity into account, the reflectivity of the graphene diaphragm should be nearly twice of fiber endface. The relationship between the different thickness of graphene and reflectivity is shown in Fig. 4(a). It can be seen that the reflectivity is about 7% when the thickness of the graphene diaphragm is 10nm. Hence, the thickness of graphene diaphragm is selected as 10nm in whole experiment. In addition, the contrast of the spectrum relies on the cavity length, which should be precisely adjusted. The sensor head and its tail fiber are respectively fixed on the horizontal platform and alignment jig, and kept at the equal altitude. Afterwards the cavity length can be freely adjusted with a 10μm step. When the cavity length is less or higher than the maximum contrast point, the spectrum is not optimal due to the reflectivity mismatch of the two mirrors. Once the cavity length is adjusted at the optimum state, the tail fiber will be fixed by the above mentioned method of Fig. 3(d). The optimal reflection spectrum of EFPI is presented in Fig. 4(b), and the contrast and FSR are respectively approximate 18dB and 20nm in air. Furthermore, the underwater spectrum also needs to be acquired to conduct the underwater acoustic experiment. The contrast will decrease when the fabricated sensor head is placed into the water owing to the imbalance of pressure inside and outside the air cavity. The cavity length is respectively figured out which is 62.1μm and 50.8μm in the air and water. The red line shows that the contrast and FSR are respectively about 14dB and 25nm.

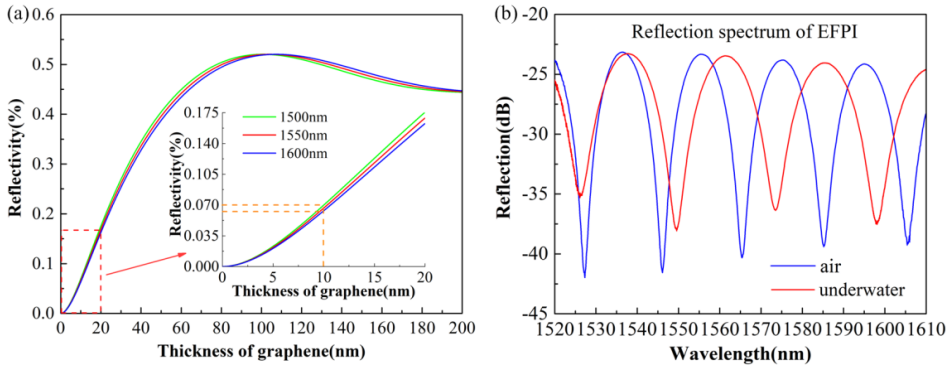

Fig. 4. (a) The relationship between the different thickness of graphene and reflectivity. (b) The transmission spectrum of EFPI in air and underwater.

Optics EXPRESS

4. Experimental results and discussions

According to the analysis of section 3, the fixed sensor head can be tested not only in the air, but also underwater. The schematic diagram and part of the experimental setup of the whole acoustic test system in the air and underwater are exhibited in Fig. 5. The experimental apparatus mainly includes 1570nm DFB laser source (long-term stability:≤ ± 0.02dB), optical fiber circulator (OFC), photoelectric detector (PD, New Focus 1623), acoustic generator (B&K, WB-3570), ultrasonic sound source (Core morrow, 156kHz), ultrasonic actuator (Core morrow, E01), DC coupled actuator (B&K, WQ-3205), processor (B&K, LAN-XI 3160) and standard microphone (B&K, 4193-L-004). The light emitted by the laser source reaches the sensor head through the port 1 and 2 of OFC. Afterwards the modulated optical signal is reflected into the PD through the port 2 and 3 of OFC. Finally, the periodically modulated signal is recovered on the PC after being processed. The acoustic signal from infrasound to ultrasound can be implemented by the acoustic generator and ultrasonic sound source, and the acoustic frequency is controlled by the signal generator integrated on the processor. Furthermore, the standard microphone is selected to calibrate in the air, and the underwater calibration requires standard hydrophone.

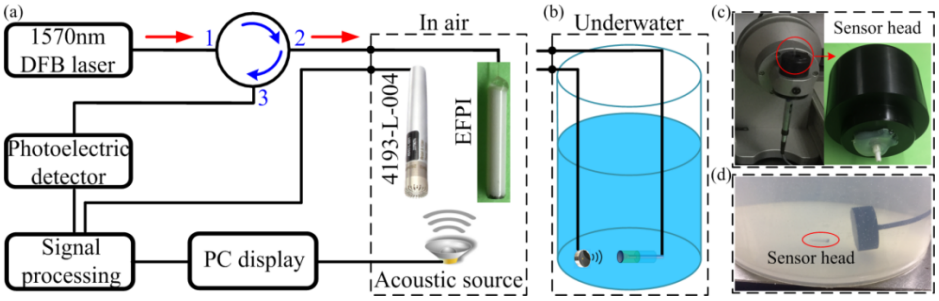

Fig. 5. The schematic diagram of the whole acoustic test system (a) in air and (b) underwater; (c) Infrasound generator and fabricated sensor head; (d) Ultrasonic sound source and sensor head underwater.

The ultra-wideband acoustic test is conducted from infrasound to ultrasound. Before the underwater test, the fixed sensor head was placed into the low frequency comparison coupler. As illustrated in Fig. 5(c), the graphene diaphragm sensor head is glued onto an adaptor with a 0.5 inch open hole. Then the whole fixed structure is inserted into the coupled cavity in which the low frequency acoustic field is generated. The above mentioned standard microphone is directly screwed into the low frequency coupled cavity for infrasound calibration and comparison. It should be noted that the coupled cavity is totally enclosed. Once the acoustic field is generated, the time domain waveform and its Fourier transform will be displayed simultaneously on PC. The infrasound of 5Hz and 15Hz has been tested, and the results are shown in Figs. 6(a) and 6(b). The drive voltage is 1Vrms, and the corresponding acoustic pressure is 10Pa (sound pressure level: 114dB). It can be seen that the signal to noise ratio (SNR) is only 20dB at 5Hz, and the resolution bandwidth is 1.67Hz. As a result, the MDP of 0.77Pa/Hz$^{1/2}$@5Hz is figured out, which is located at the lower level. The evaluation index shows the low frequency noise is high. The reason is mainly caused by power fluctuation of laser source, the slight variation of external temperature and the weak vibration of instrument. Moreover, the audible frequency of 150Hz and 2kHz has been measured in air by the calibration of sound level meter. As exhibited in Figs. 6(c) and 6(d), both of the two detected frequencies have a SNR of 35dB, and the applied sound pressure is the same value. In other words, the aforementioned two audible frequencies are located at the same noise level, and have the identical MDP. None of the above measurement frequencies in the air is within the scope of ultrasound. On the basis of section 3, the fabricated sensor head still has a good interference pattern after being placed into water. Additionally, the 1570nm laser

Optics EXPRESS

wavelength should also be situated near the quadrature working point of the interference spectrum. As depicted in Figs. 5(b) and 5(d), the sensor head is placed opposite to the ultrasound source at the bottom of the bucket, and the distance is about 1cm. As can be seen in Figs. 6(e) and 6(f), the ultrasound of 50kHz and 800kHz can be detected underwater. Thence, the proposed sensor head has realized the measurement range of acoustic frequencies from infrasound to ultrasound in air and underwater.

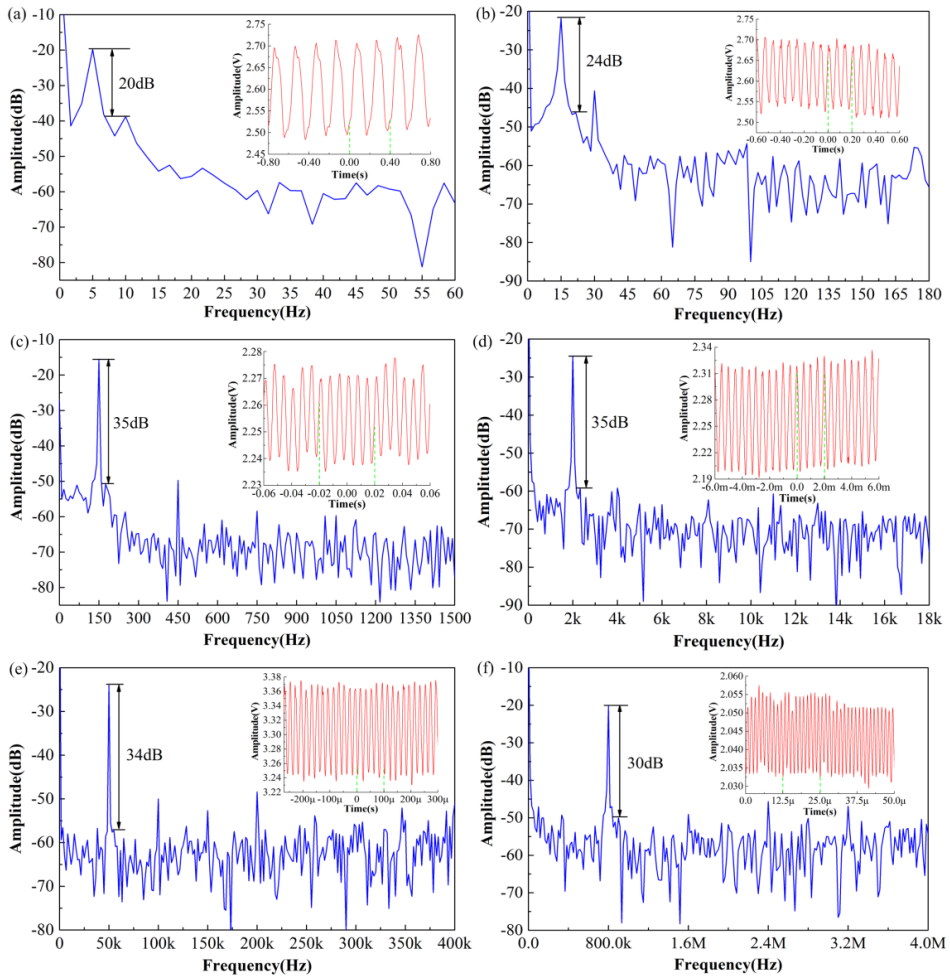

Fig. 6. The experimental results of acoustics test from infrasound to ultrasound, and the time domain waveform reflected in illustration. The single frequency experimental results are respectively (a) 5Hz, (b) 15Hz, (c) 150Hz, (d) 2kHz, (e) 50kHz, (f) 800kHz. (a)~(d) tested in the air, (e) and (f) detected underwater.

The range of flat response has a great of significance in acoustic sensing. From the analysis of section 2, the region of flat response is mainly dependent on the resonant frequency of graphene diaphragm which has a theoretical value of 101.4Hz. However, pre-bending of the diaphragm leads to the effective area less than the designed value. Thus, the practical value of resonant frequency is slightly higher than 101.4Hz. In this case, the flat response range contains two segments. One is located at low frequency infrasound, and the other frequency band is over kHz. As indicated in Fig. 7, the frequency band of infrasound has a relatively weak response, while they have close SNR at the same sound pressure. So the frequency band of infrasound can be regarded as flatness. Similarly, the frequency band above kHz can also be considered flat due to the same sound pressure applied underwater.

Optics EXPRESS

The applied sound pressure is 68.5dB when the measurement frequency is 10kHz, and the corresponding SNR and resolution bandwidth are 34dB and 833.3Hz. So the MDP of 33.97μPa/Hz1/2@10kHz can be acquired. There are a larger response of 60Hz and 150Hz because they are close to the resonant frequency.

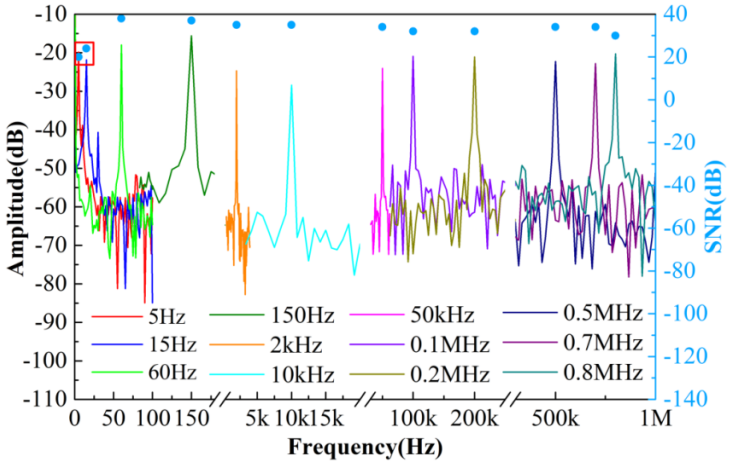

Fig. 7. Fourier transform of different frequencies from infrasound to ultrasound and its corresponding SNR. The frequency over 50kHz is monitored underwater, and below 15kHz is tested in the air

The same single frequency is also tested both in air and underwater to verify the effect of acoustic transmission media on sound measurement. Both of the sound source and sensor head are the same in air and underwater. As demonstrated in Fig. 8(a), the measurement effect of 2kHz in air is obviously superior to underwater. Though they have the same SNR, the harmonic component of underwater is larger than that in air. Besides, the noise level is also higher. The reason is owing to the relatively longer propagation wavelength underwater that the acoustic wave of underwater is easier to diffract than that in air during the measurement. Meanwhile, the experiment of 100kHz is also conducted, as presented in Fig. 8(b). It is apparent that both the time domain waveform and the Fourier transform of underwater are better than those in air. This is mainly dependent on the acoustic impedance. In the fields of acoustic measurement, the sound velocity is inversely proportional to acoustic the impedance when the sound pressure is constant. Therefore, the acoustic impedance of water is less than that of air due to its higher sound velocity. Moreover, it can be found that the SNR of 100kHz is higher than that of 2kHz under the same drive voltage of sound source by comparing Figs. 8(a) and 8(b). This phenomenon is caused by the different water pressures. According to the theory of ultrasound measurement, the vibration frequency, medium density and sound velocity are all proportional to the sound pressure, as deduced in the following Eq. (6).

$$P = \rho_m v_s x \omega_s \tag{6}$$

where P is the sound pressure emitted from acoustic source. ρ_m, v_s, x and ω_s are respectively the medium density, sound velocity, amplitude of mass point and vibration frequency. Combine the results of Figs. 8(a) and 8(b) and the ultrasonic measurement theory, frequencies above ultrasound are more suitable for underwater measurement, and the other frequency bands are more applicable to be monitored in the air.

Optics EXPRESS

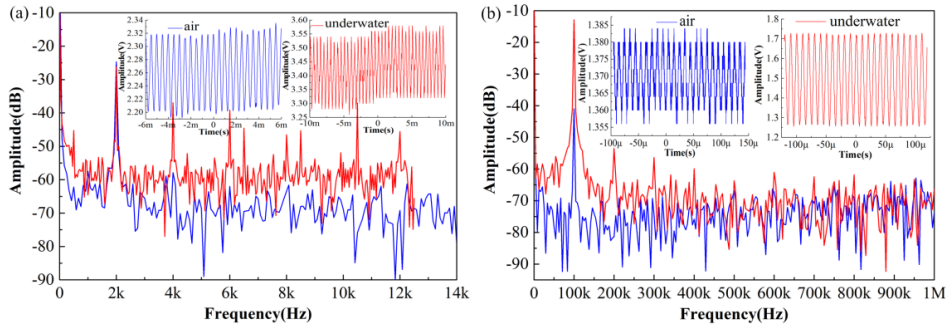

Fig. 8. Comparison of the same frequency in air and underwater. (a) 2kHz. (b) 100kHz.

5. Conclusions

In summary, the proposed FOAS has an ultra-wideband response range from 5Hz to 0.8MHz. The transduction material is the ultrathin graphene diaphragm with the thickness of 10nm. Moreover, the air cavity of EFPI structure is like a horn-shape, and the radius of open hole is 1mm. The proposed sensor head can realize acoustic measurement from air to underwater after encapsulation. The flat response region has two segments which are respectively in the frequency band of infrasound and above kHz, and the MDP of 0.77Pa/Hz$^{1/2}$@5Hz and 33.97μPa/Hz$^{1/2}$@10kHz can be achieved. The experimental results indicate that frequencies above and below ultrasound are more suitable for underwater and in air measurement, respectively. Other merits of the proposed sensor are its compact size of 14mm and cost-effective. Overall, the proposed FOAS is believed to have a bright application prospect.

Funding

National Natural Science Foundation of China (NSFC) (61775070, 61275083); a grant from the Fundamental Research Funds for the Central Universities (2017KFYXJJ032, 2017KFXKJC002).